An amphipathic helix enables septins to sense micron-scale membrane curvature

Kevin S. Cannon[1], Benjamin L. Woods[1], John M. Crutchley[1], and Amy S. Gladfelter[1,2]

1. Department of Biology, University of North Carolina at Chapel Hill, NC
2. Marine Biological Laboratory, Woods Hole, MA

Corresponding author: amyglad@unc.edu

Keywords: septin, curvature sensing, amphipathic helix

Abstract

The geometry of cells can be well described by membrane curvature. Septins are filament forming, GTP-binding proteins that assemble on positive, micrometer-scale curvatures. Here, we examine the molecular basis of septin-mediated curvature sensing. We show that differences in affinity and the number of binding sites drive curvature-specific adsorption of septins. Moreover, we find septin assembly onto curved membranes is cooperative and show that geometry influences higher-order arrangement of septin filaments. Although septins must form polymers to stay associated with membranes, septin filaments do not have to span micrometers in length to sense curvature, as we find that single septin complexes have curvature-dependent association rates. We trace this ability to an amphipathic helix located on the C-terminus of Cdc12. We conclude that this domain is necessary and sufficient for curvature sensing both *in vitro* and *in vivo*. These data show that curvature sensing by septins operates at much smaller length scales than the micrometer curvatures being detected.

Introduction

Shape is a fundamental feature in cell biology. The relationship between form and function within cells and many of their internal compartments are often dependent on the lipid membrane that surrounds them, and can be thought of in terms of membrane curvature (Zimmerberg and Kozlov, 2006; Cannon, Woods and Gladfelter, 2017). How do cells use nanometer-sized components to perceive micron-scale changes in shape?

Septins, are filament-forming, GTP-binding proteins found to localize to sites of micron-scale membrane curvature from yeast through humans (Field *et al.*, 1996; Pan, Malmberg and Momany, 2007; Bridges *et al.*, 2016). Examples of curvature-associated localizations include the bud-neck in *S. cerevisiae* (Byers and Goetsch, 1976; Haarer and Pringle, 1987; Ford and Pringle, 1991), bases of dendritic spines in neurons (Cho *et al.*, 2011), branches in filamentous fungi (Westfall and Momany, 2002; DeMay *et al.*, 2009; Bridges *et al.*, 2016), and the cytokinetic furrow (Spiliotis, Kinoshita and Nelson, 2005; Joo, Surka and Trimble, 2007; Maddox *et al.*, 2007). At these sites, septins coordinate cell cycle progression (Longtine *et al.*, 2000; Sakchaisri *et al.*, 2004), influence lateral diffusion in the membrane (Clay *et al.*, 2014; Yamada *et al.*, 2016), and act as a scaffold to recruit proteins required for chromosome segregation (Spiliotis, Kinoshita and Nelson, 2005) and cytokinesis (Meitinger *et al.*, 2011; Finnigan *et al.*, 2015). Septins carry out these many functions by assembling into heteromeric, rod-shaped, non-polar complexes which can anneal end-on to polymerize into filaments at the plasma membrane (Field *et al.*, 1996; John *et al.*, 2007; Sirajuddin *et al.*, 2007; Bertin *et al.*, 2008). Budding yeast possess five mitotic septins that assemble into hetero-octamers in which the terminal subunit is either Cdc11 or Shs1(Garcia *et al.*, 2011; Khan, Newby and Gladfelter, 2018). Purified recombinant septins from yeast and humans were shown to preferentially adsorb onto micrometer curvatures in the absence of any cellular factors (Bridges *et al.*, 2016) indicating that curvature sensing is an intrinsic and conserved feature of the septin cytoskeleton. The mechanism underlying how septins sense micron-scale membrane curvature is unclear.

Most of what we know about curvature sensing comes from nanometer-sized molecules interacting with nanometer-scale curvatures. Proteins containing BAR domains or amphipathic helices utilize combinations of membrane insertion (Drin and Antonny, 2010), oligomerization, and scaffolding mechanisms (Simunovic, Srivastava and Voth, 2013; Simunovic *et al.*, 2015) to either sense or deform the local curvature. The high curvatures on the nanometer scale generate

lipid packing defects within the membrane, providing binding sites for amphipathic helices (Hatzakis *et al.*, 2009). This mechanism is used by several proteins to sense curvature including α-synuclein (Pranke *et al.*, 2011), magainin (Matsuzaki, 1998; Drin and Antonny, 2010), and ArfGAP1 (Drin *et al.*, 2007); however, the diverse physicochemical properties between amphipathic helices greatly influences membrane binding and curvature sensitivity by these proteins. Additionally, protein oligomerization and higher order structure (e.g. lattice) formation onto curved surfaces can be used to match the local curvature or impart new membrane curvature. Interestingly, curvature sensors on the micrometer-scale including SpoVM (Ramamurthi *et al.*, 2009), MreB (Ursell *et al.*, 2014; Hussain *et al.*, 2018), and septins (Bridges *et al.*, 2016) either contain amphipathic helices, polymerize, or both. However, detailed mechanisms remain to be elcuidated. SpoVM uses an affinity-based mechanism, dependent on an 11-amino acid amphipathic helix to accumulate at specific membrane curvatures. It is unknown how septins, the only identified eukaryotic micrometer-scale curvature sensor, preferentially accumulate at specific membrane geometries.

In this study, we investigate the mechanisms of septin curvature sensing. We find that affinity and number of available binding sites drive preferential septin assembly onto membranes of specific curvatures. Using supported lipid bilayers on both beads and rods, we find that septin assembly on membranes is a highly cooperative process and that short filaments align according to curvature. Additionally, we find that single septin oligomers bind with different rates depending on the curvature. Finally, we uncovered a conserved amphipathic helix within the C-terminus of the yeast septin Cdc12 that is both necessary and sufficient for curvature sensing by septins. Thus, this study provides the first insights into the molecular basis for how septins sense curvature.

Results and Discussion

Septins bind cooperatively to curved membranes with differences in affinity and maximal binding

We previously identified that the septin cytoskeleton preferentially adsorbs onto specific micrometer-scale membrane curvatures *in vitro* and *in vivo* (Bridges 2016). To understand the biochemical basis for distinguishing amongst different curvatures, we preformed saturation binding isotherms and measured septin binding onto supported lipid bilayers (SLBs) of various curvatures. Septins have the strongest affinity for 1 µm beads (curvature, $\kappa = 2\ \mu m^{-1}$, K_d 13.5

nM), followed by 3 µm beads (κ= 0.67 μm^{-1}, K_d 18.5 nM), and 0.5 µm beads (κ= 4 μm^{-1}, K_d 34.3 nM) (Figure 1) (Table 1). Additionally, the difference in maximal binding capacity (B_{max}) is dramatically different for tested bead sizes, indicating that there are curvature-dependent differences in the number of effective binding sites for septins (Figure 1) (Table 1). This is not simply due to differences in surface area on different bead sizes because adsorption is normalized for surface area. Additionally, saturation binding curves had Hill coefficients of 2.6 (κ= 4 $\mu m^{-1}$and κ= 0.67 μm^{-1}) and 2.9 (κ= 2 μm^{-1}), indicating septin adsorption on all tested membrane curvatures is highly cooperative. Consistent with our previous observations, we noticed septins accumulated onto some beads, while neighboring beads were void of any septins (Figure 1), suggesting that initial septin recruitment to curved membranes can positively influence subsequent septin binding.

We speculate that there might be different concentration-dependent regimes of curvature sensitivity by septins: affinity might be the major driver at lower septin concentrations; whereas at higher concentrations when filaments become longer or densely packed, the contribution of B_{max} to curvature sensitivity might increase depending on how filaments can arrange on different curvatures. Collectively, these data suggest that differences in septin affinity and the number of available binding sites can drive preferential assembly of septins onto specific curvatures in a cooperative fashion.

Septin filament orientation is dependent on membrane curvature

Cooperativity in assembly could arise at multiple scales, from filament formation to lateral associations between filaments or other higher-order structures including layers of filaments. To investigate how septins cooperatively assemble on membranes we adapted the SLB bead-based assays to rods in which septins are incubated with a range of membrane curvatures and visualized filament arrangement using scanning electron microscopy (SEM). By varying septin concentrations in the assay, we could control septin-filament regimes: from short septin filaments across the rod surface to tightly packed higher-order assemblies with lateral associations, bundling, or lattices. To evaluate how cooperativity may arise at the level of polymerization, we first asked how long a septin filament needed to be to align along optimum curvature.

We scored the length and orientation of filaments on a range of rod diameters binned to three categories (100-400 nm, 401-600 nm, and 601-1000 nm). For all three categories, we found

that septin octamers (32 nm in length, a single octamer) sampled a wide variety of orientations along the rod (Figure 2). Furthermore, on rod diameters ranging from 401-600 nm, we saw no preferential orientation as a function of filament length and instead observed a wide distribution of orientations. This likely reflects septin filaments dynamically sampling a range of membrane curvatures and is momentary glimpse at the time of fixation. However, on rod diameters from 100-400 nm and 601-1000 nm, the orientation of filaments relative to the axis of principal curvature became evident as a function of filament length. For rod diameters of 600-1000 nm, septin filaments 64 nm long (two annealed octamers) show a tendency to align along the axis of principal curvature. In contrast, for the rods with diameters spanning 100-400 nm, 64 nm filaments become aligned to the long-axis (axis of zero curvature) of the rod presumably avoiding the higher positive curvature on these narrow rods. This reinforces our previous report in which septins preferentially bind membranes with positive curvature, and that they avoid high and negative membrane curvature (Bridges *et al.*, 2016). Once filaments were 3-4 octamers long, these trends in alignment became even more evident (Figure 2). Despite the tendency of septins to align towards or away from the principal curvature depending on rod diameter, there are large deviations in filament alignment at all measured filament lengths (Figure 2) (Table 2). This indicates that the ultimate alignment on a given curvature requires either longer septin filaments or lateral interactions that are not achieved at the lower septin concentration used in this experiment (Figure 2). These data suggest that ability of septins to sense curvature can be detected even with the shortest of septin filaments, made of only two oligomers.

We next examined septin filament orientation at higher protein concentrations to examine how densely packed septin assemblies align relative to membrane curvature. At higher concentrations (50-500 nM) septin filaments were tightly packed, and generally aligned with each other (Figure 3). On rod diameters ranging from 100 nm to 400 nm, septin filaments consistently aligned parallel to the long axis of the rod. For rod diameters ranging from ~400 nm through ~ 630 nm, we noticed that septin filaments exhibit a wide range of orientations, consistent with what we saw in the low density septin regime for this range of rod diameters. Although, neighboring filaments have a tendency to align with one another. Lastly, for rod diameters ranging from ~ 670 nm through 2300 nm, septin filaments become closely aligned to the axis of principle curvature (Figure 3). Due to limitations in available rod sizes, we did not test rod diameters higher than 2300 nm. Thus, at high density, septin filaments even more closely

match the curvature of the rod than septin filaments under a low-density regime and become less variable in their orientations.

These data suggest that the ability of septins to perceive micron-scale curvature may also be in part driven by septin filament density. We imagine filament density could influence septin filament orientation in two ways, which are not necessarily mutually exclusive. First, aligned septin filaments in close proximity to each other might be stabilized by lateral interactions with one another. In support of this idea, septin filaments have been observed to pair and bundle *in vitro* by EM (Frazier *et al.*, 1998; Bertin *et al.*, 2008; Sadian *et al.*, 2013). Secondly, we imagine that tightly packed septins might sterically hinder one another, thus in aggregate "enforcing" alignment along the optimal curvature. This is best observed in the smaller dimeter rods (100-400 nm; see Figure 3), in which long filaments are aligned with one another but not necessarily touching. Nonetheless, at higher septin concentrations, filaments are also *longer* on rods than at low concentrations. Thus, we cannot discount the possibility that filament length is the major driving factor for septin filament orientation in this assay, rather than lateral filament associations or steric hindrance via filament packing.

Single septin complexes have a higher association rate for optimal membrane curvatures

We next wanted to assess the basis for curvature-dependent septin affinity differences and determine the length scale at which affinity differences may arise. It is striking that short oligomers consisting of two hetero-octamers have a biased orientation on rods and is consistent with our previous work suggesting non-polymerizable septins distinguish different sized beads. However, a caveat to interpretation of our previous report that used non-polymerized complexes is that artificial tethering of septins to SLBs via nickel-His recruitment was required and this likely bypasses native protein-membrane interactions mechanisms. As a different approach, we examined the kinetics of membrane-association for single septin oligomers without artificial tethering, using near TIRF microscopy to measure binding and unbinding events of single septin hetero-octamers, determined based on single-step photobleaching calibration, on various curvatures (Figure 4 and Supplemental figure 1).

We measured the number and duration of these binding events to calculate association and off rates for single septin complexes on curvatures of 2 μm^{-1} and 0.67 μm^{-1} (Figure 4). Histograms of dwell times for single septin-complex binding events were fit to a single exponential decay function. The measured dwell times for these curvatures were 0.21s ± 0.019

and 0.21 ± 0.023, for $\kappa = 2\ \mu m^{-1}$ and $\kappa = 0.67\ \mu m^{-1}$, respectively ($N_{particles\ per\ curvature} > 150$). The observed dwell times correspond to a high off-rate, supporting previous observations that a single septin hetero-octamer does not stably associate with membranes (Bridges *et al.*, 2016). Notably, the measured dwell times were the same on both curvatures tested, suggesting that curvature does not influence how long a single septin complex remains associated with the membrane. In contrast, on curvatures of $\kappa = 2\ \mu m^{-1}$ we observed a septin association rate of 0.061 $\mu m^{-2}s^{-1}nM^{-1}$, whereas for $\kappa = 0.67\ \mu m^{-1}$, we observed a septin association rate of 0.025 $um^{-2}s^{-1}nM^{-1}$ (Figure 4). Thus, there are markedly different association rates of septins for different curvatures.

The ~2.5-fold difference in association rate between these two curvatures was striking, given that our saturation binding isotherms show K_d values so close to one another (13.5 and 18.5 nM, respectively). This could be explained by the fact that our binding curve data is a summation of several reactions: initial septin-membrane binding, annealing and fragmentation events, and septin-filament lateral interactions, all of which may be influenced by the local curvature and contribute to the K_d estimates in this experiment; whereas the single molecule near-TIRF assay allows us to observe the initial septin-membrane binding and unbinding reactions in the absence of the other confounding reactions. These results suggest that even a single septin octamer can detect curvature differences through the initial association with the curved membrane via the association rate, but not the off rate. This also indicates that there must be a curvature-dependent bilayer defect being perceived by septin octamers even at this shallow, micron-scale curvature.

The C-terminus of Cdc12 has an amphipathic helix domain that is necessary and sufficient for curvature sensing

How can the association rate of a single septin octamer be sensitive to curvature on the micron scale? Many proteins that sense nanometer scale curvatures contain membrane-binding amphipathic helices(Drin *et al.*, 2007)(Drin and Antonny, 2010), however, the degree to which these motifs function as membrane binding vs. curvature sensitive or curvature inducing domain is context dependent (Drin and Antonny, 2010; Madsen *et al.*, 2010; Chen *et al.*, 2016). Interestingly, another micron scale curvature sensor, SpoVM, a 26-amino acid polypeptide, utilizes an 11-residue amphipathic helix to sense curvature (Gill *et al.*, 2015) and also shows curvature-dependent association rates (Kim *et al.*, 2017). We searched for AH motifs in septin

sequences and found conserved, predicted amphipathic helices at the C-termini of a subset of septins (Figure 5). Despite being amphipathic and similarly situated within the primary sequence, there are significant differences in the net charge and hydrophobicity between septins from different species (Supplemental figure 3). We hypothesized that the AH may contribute to membrane binding and possibly confer specificity to curved membranes.

Interestingly, the AH domain of Cdc12 is truncated within a classic temperature sensitive septin mutant, *cdc12-6* (Johnson *et al.*, 2015) (Figure 5). In these mutants, septins localize normally to the bud-neck at permissive temperature, but rapidly disassemble and disassociate from the membrane in response to a shift in temperature (Gladfelter *et al.*, 2005). At restrictive temperatures, *cdc12-6* mutants arrest, unable to complete cytokinesis. First, we evaluated if the AH was necessary for curvature sensing by examining if recombinant septins with octamers harboring the Cdc12-6 truncation could bind membranes and distinguish between different membrane curvatures. We found that Cdc12-6 mutant complexes bound all tested membrane curvatures indiscriminately in contrast to wild-type septins (Figure 5). This suggests that AH of Cdc12 is not required for septin membrane association, per se, but rather is a critical domain in specifying septin membrane association as it relates to curvature.

Next, we probed whether the AH of Cdc12 was capable of distinguishing between membrane curvatures by itself. We purified a polypeptide with two copies of the AH, to mimic the stoichiometry of the intact septin complex which has two copies of Cdc12. We found that this tandem AH polypeptide adsorbed onto membrane curvatures of 6.67 μm^{-1}, 4 μm^{-1}, and 2 μm^{-1} equally (albeit significantly less than full septin complexes, which can polymerize), while showing reduced binding to membrane curvatures of 0.67 μm^{-1} and 0.4 μm^{-1} (Figure 5). These results indicate that a conserved but previously unidentified amphipathic helix is capable of both binding to membranes and sensing membrane curvature.

Finally, we assessed the functionality of the Cdc12 AH in cells. At the base of a shmoo (a polarized yeast cell mating projection in response to pheromone) septins assemble into a collar (Giot and Konopka, 1997). In some cells, the shmoo will reorient during polarized growth creating positive membrane curvature near the base of the protrusion. As reported previously, septins in these curved cells will preferentially localize on the side of positive membrane curvature (Kelley *et al.*, 2015; Bridges *et al.*, 2016). We hypothesized that septins would no longer localize exclusively to the side of positive curvature in shmoos of *cdc12-6* mutants.

Surprisingly in these mutants septins did *not* assemble into a collar at all, but were instead either completely cytoplasmic, localized to distal cortical sites from the mating projection, or formed bulky filaments in the cytosol (Figure 5). Interestingly, in neighboring *cdc12-6* mutants that overcame the pheromone arrest, septins localized normally to the bud neck, suggesting other septin-interacting proteins may be responsible for appropriate recruitment to the bud-neck. This unexpected result suggests that the amphipathic helix in Cdc12 is required for septin localization and assembly at the base of the shmoo.

Conclusion

In this study, we examine the basis of micron-scale curvature sensing by septins. We identify a mechanism that uses both affinity and the number of available binding sites to drive curvature-specific accumulation of septins. We also highlight that cooperativity seems to be an inherent feature of septin assembly onto curved surfaces. We found that septins must polymerize to properly align towards optimal principal curvature. However, the ability for septin filaments to begin aligning towards the principal curvature is not dependent on forming filaments that are micrometers long. Remarkably, septin filaments that are only 64-nm long (2 annealed octamers) preferentially align towards positive curvatures that are orders of magnitude larger than their size. Even a single septin octamer is capable of detecting changes micrometer scale curvatures manifested by differences in association rates. We found that an amphipathic helix located within the very C-terminus of Cdc12 is necessary and sufficient for septins to distinguish different curvatures. Much of what we know about amphipathic helices comes from studies investigating nanometer-sized proteins sensing nanometer-scaled curvatures; however, it is emerging that this motif is also used by proteins to detect micrometer-scale changes in curvature. Remarkably, the bacterial micron-scale curvature sensor SpoVM is primarily composed of an AH and also shows different association rates depending on curvature suggesting this is a mechanistically conserved process. How the AH interacts with the membrane to detect curvature requires further investigation. Collectively, we show that curvature sensing by septins occurs at both the single octamer and filament levels.

Materials and Methods

Yeast septin purification

BL21 (DE3) *E. coli* cells were transformed using a duet expression system (Bridges 2016) and selected with ampicillin and chloramphenicol. Selected cells were cultured to an $O.D._{600\ nm}$ between 0.6 and 0.8 and induced with 1 mM of IPTG. Induced cultures were grown for 24 hours at 22° C (3 hours for Cdc12 amphipathic helix construct) before harvesting. Cultures were pelleted at 10,000 RCF for 15 min. Pellets were resuspended in lysis buffer (1M KCl, 50 mM, Hepes pH 7.4, 1 mM $MgCl_2$, 10% glycerol, 1% Tween-20, and 1x protease inhibitor tablet (Roche), 20 mM Imidazole, 1 mg/mL lysozyme) for 30 minutes on ice with intermittent vortexing. The lysate was sonicated twice for 10 seconds and clarified by centrifugation using an SS-34 rotor at 20,000 RPM for 30 minutes. Clarified supernatant was filtered using 0.44 μm filter, then incubated with equilibrated Nickel-NTA^{2+} or Cobalt resin (Thermo Fisher Scientific; 2 mL resin per liter of *E.* coli culture) at 4°C for 1 hour. Resin and lysate were added to a gravity flow column. Bound protein was washed four times with 5x the column volume with wash buffer (1M KCl, 50 mM Hepes pH 7.4, 20 mM Imidazole), and then eluted in elution buffer (300mM KCl, 50 mM Hepes pH 7.4, 500 mM Imidazole). Eluted protein was then dialyzed into septin storage buffer (300 mM KCl, 50 mM Hepes pH 7.4, 1 mM BME) for 24 hours in two steps (Slide-A-Lyzer G2 20K MWCO, Thermo Fisher Scientific; 10K MWCO for amphipathic helix constructs). During dialysis, 60 μg of TEV protease (Sigma) was added to cleave the 6x-histidine tag on Cdc12. 24 hours later, the protein was run over a second column (either Ni-NTA or cobalt resin) to remove the protease, the poly-histidine tag, and additional contaminants. Protein purity was determined via SDS-PAGE and protein concentration was determined via Bradford assay.

Lipid mix preparation

All septin binding experiments were done using supported lipid bilayers consisting of 75 mol % dioleoylphosphatidylcholine (DOPC) Avanti Polar Lipids, 25 mol % phosphatidylinositol (PI) (Liver, Bovine) sodium salt, and trace amounts (less than 0.1%) of phosphatidylethanolamine N(lissamine rhodamine B sulfonyl) (Rh-PE) (ammonium salt) Egg-Transphosphatidylated, Chicken) (Avanti Polar Lipids 810146). Lipids were mixed in chloroform solvent, and dried by a stream of argon gas to generate a lipid film. Remaining solvent was evaporated by placing the lipid film under a vacuum for at least 6 hours. Lipids were rehydrated in supported lipid bilayer

buffer (300 mM KCl, 20 mM Hepes pH 7.4, 1 mM $MgCl_2$) for 30 minutes at 37°C to give a final concentration of 5 mM. Hydrated lipids were subject to vortex for 10 seconds, every 5 mins for 30 mins bath sonicated in 2 minute intervals until clarification to yield small unilamellar vesicles (SUVs).

Preparation of supported lipid bilayers on silica microspheres

SUVs were adsorbed onto silica microspheres (Bangs laboratories) of various curvatures by mixing 50 nM lipids with 440 um^2 of silica microsphere surface area or 10 uL of rods in a final volume of 80 uL for 1 hour on a roller drum at room temperature. Unbound lipid was washed away by pelleting lipid-coated beads at the minimum force required to pellet each bead size using pre-reaction buffer (33.3 mM KCl, 50 mM Hepes pH 7.4) (See http://www.bangslabs.com/ for sedimentation speeds). Washes were preformed 4 times.

Measuring protein adsorption onto silica microspheres

To examine septin adsorption onto different membrane curvatures, 25 µL of septins in septin storage buffer were added to 75 µL of a bead-buffer solution of 5 mm^2 total lipid-bead surface area to give a final buffer composition of 100 mM KCl, 50 mM Hepes pH 7.4, 1 mM BME, 0.1% methylcellulose, and 0.1% bovine serum albumin (fatty acid free- Sigma). Saturation binding curves were obtained using several different septin concentrations in simple mixtures, containing only one bead size per reaction volume. Amphipathic helix adsorption was measured in mixtures containing protein and various bead diameters. Each reaction was incubated in a plastic chamber (Bridges methods paper) glued to a polyethyleneglycol (PEG)-passivated coverslip for 1 hour (to allow the reaction to reach equilibrium). Beads were imaged using either a wide-field microscope with a Ti-82 Nikon stage a 100x Plan Apo 1.49 NA oil lens, and Zyla sCMOS (Andor) (saturation binding curves) or a spinning disc (Yokogawa) confocal microscope (Nikon Ti-82 stage) using a 100x Plan Apo 1.49 NA oil lens, and a Prime 95B CMOS (Photometrics) (amphipathic helix and Cdc12-6 septin complex adsorption experiments). For analysis of septin binding, raw images were exported into Imaris 8.1.2 (Bitplane AG, Zurich, Switzerland). Each image was background subtracted in both channels using the software's Gaussian filter for background determination (width 31.4 µm). The surface of each bead was defined using the lipid channel. Using the surface generate on each bead, sum intensity values from lipid and septin channels were exported from Imaris into Microsoft Excel. Septin adsorption was calculated by dividing the multiple sum intensity values from the septin channel

over the sum intensity values from the lipid channel as to control for surface area for each bead size. Boxplots were generated through exporting intensity sum values from both channels into R version 3.2. 2 (R Foundation for Statistical Computing, Vienna, Austria, using RStudio 0.99.467, Boston, MA, USA). Boxplots were generated using ggplot2 package (Wickham, 2007; Wickham, 2009; Winston, 2014).

Generation and preparation of septin-rod supported lipid bilayer mixture.
Borosilicate rods were obtained from Glass Microfiber filters, GFC, 42.5 mm (Whatman). A single filter was torn up into small pieces into a beaker with 60 mL of 100% ethanol and sonicated until the solution became opaque. The solution was stored at room temperature overnight. The next day, 10 µL of rods were taken from the solution after thorough mixing. 70 uL of SLB buffer was added to the rods and spun down at top speed to dilute the ethanol in the solution. This step was repeated 4 additional times. 5 mM of SUVs (75% DOPC, 25% PI, trace Rh-PE, as described above) were added to the polycarbonate rods and allowed to incubate for 1 hour at room temperature. Unbound lipid was washed away pelleting lipid-coated beads at top speed (16.1 RCF) using pre-reaction buffer. The mixture of septin-lipid-coated rods were added to a circular 12mm (PEG)-coated coverslips and incubated at room temperature for 1 hour and then and prepared for scanning electron microscopy.

Scanning electron microscopy
The septin-rod mixture onto a circular PEG-coated 12mm coverslip, was fixed in 2.5% glutaraldehyde in 0.05 M sodium cacodylate (NaCo) pH 7.4 for 30 minutes followed by 2x washes in 0.05 M NaCo (5 min each wash). Samples were post-fixed in 0.5% OsO_4 Cacodylate buffer for 30 minutes and washed 3x in NaCo (5 minutes each wash). Samples were then incubated with 1% tannic acid for 15 minutes followed by 3x washes in NaCo. 0.5% OsO_4 was added for 15 minutes followed by 3x washes in NaCo. Samples were then dehydrated with increasing ethanol concentrations: (30% EtOH for 5 minuets, 2x; 50% EtOH for 5 minutes; 75% EtOH for 5 minutes; 100% EtOH for 5 minuetes, 2x followed by another 10 minute incubation). Samples were incubated in transition fluid (hexamethyldisilazane) 3x; (incubation times: 5 minutes, 10 minutes, 5 minutes) and were allowed to airdry and then placed in a desiccator until sputter coating. Samples were coated in a gold/palladium alloy and then imaged on a Zeiss Supra 25 Field Emission Scanning Electron Microscope.

Kinetics of single septin complex onto lipid-coated beads

Two PEG-passivated coverslips were sandwiched together using double-coated pressure sensitive adhesive tape (Nitto product:5015ELE) to make narrow (~20 µL flow chambers). A mixture of septins and lipid-coated beads of a given diameter were then flowed through the chamber and imaged using near-total internal reflection fluorescence microscopy. The number and duration of binding events were performed manually. Association-rate was quantified by calculating the number of binding events over the product of septin concentration, time, and binding area. To ensure the off rates were not dominated by bleaching, we generated bleach profiles (Supplemental figure 1). The amount of time it took to bleach single septin complexes is much higher than the observed dwell time. Bleach steps were also used to calibrate intensity so that scored puncta were single septin complexes.

Generation of helical wheel diagrams

Helical wheels and the calculation of net charge and hydrophobic moment were generated using Heliquest (http://heliquest.ipmc.cnrs.fr).

Budding yeast alpha factor shmoo experiments

Yeast cells were grown overnight at 22°C to mid-log phase in Complete Synthetic Medium (CSM, MP Biomedicals) + 2% dextrose. MATa, *bar*- cells were treated with 500 nM alpha-factor mating pheromone (GenWay Biotech), and either remained at 22°C or were shifted to 37°C for two hours before fixation using 3.7% formaldehyde. Fixed cells were mounted onto CSM slabs solidified with 2% agarose, and imaged using a spinning disc (Yokogawa) confocal microscope (Nikon Ti-82 stage) using a 100x Plan Apo 1.49 NA oil lens, and a Prime 95B CMOS (Photometrics).

Acknowledgements

We thank the Gladfelter lab and Danny Lew for useful discussions, Matthias Garten for ideas in setting up the rod assay, the UNC EM facility (Victoria Madden and Kristen White) for support with SEM and NSF grant (MCB-5105178) to ASG.

Author contributions

KSC, BLW conducted experiments. BLW constructed strains for experiments. JMC constructed plasmids for experiments. KSC, BLW, and ASG designed experiments.

BLW helped design and performed experiments. JMC helped clone several constructs. ASG helped design experiments

Abbreviations

SLB: Supported lipid bilayer

PEG: Poly-ethylene glycol

Figure Legends

Figure 1. Septins bind cooperatively to curved membranes with differences in affinity and maximal binding

Supported lipid bilayers (75% dioleoylphosphatidylcholine (DOPC), 25% phosphatidylinositol (PI), and trace amounts of rhodamine-phosphatidylethanolamine (Rh-PE)) were reconstituted on silica beads of various curvatures (κ = 4 μm^{-1}, 2 μm^{-1}, and 0.67 μm^{-1}). Purified septins were titrated at several concentrations through saturation. (A) Representative images are maximum intensity projections of septin adsorption onto supported lipid bilayers at various septin concentrations. All images are contrasted identically. The cartoon at the top is of a GFP-tagged septin octamer. Scale bar 10 µm. (B) Quantification of septin adsorption at equilibrium onto supported lipid bilayers of varying curvature. Each data point represents the mean intensity for 98-600 beads. Error bars are SEM.

Figure 2. Septin filament alignment towards the axis of principal curvature is dependent on filament length

Supported lipid bilayers (75% DOPC, 25% PI, and trace amounts of Rh-PE) were reconstituted on poly-carbonate rods of different diameters ranging from approximately 100 nm to 2300 nm. (A-C) Representative images of septin filament alignment on rods from the three different categories. Scale bar 200 nm. (A) Rod diameter = 205 nm (B) Rod diameter = 500 nm (C) Rod diameter = 815 nm. A subset of filaments were false colored; pink filaments are more parallel to the long axis of curvature; blue filaments are oriented at ~ 45°; green filaments are aligned to the axis of principal curvature. (D) Schematic of septin filament length in terms of the number of octamers in a filament and a cartoon of how septin orientation relative to the long axis of the rod was measured. (E-G) Box and whisker plot quantifying septin filament alignment on various rod diameters as a function of filament length binned to three diameter ranges. Black bars represent the median. Error bars are standard deviation (E) 100-400 nm rods. N= 23 rods and 193 filaments (F) 401-600 nm rods. N= 15 rods and 189 filaments. (G) 601-2000 nm rods. N= 24 rods and 491 filaments

Figure 3. Septin filament orientation is dependent on membrane curvature

Supported lipid bilayers (75% DOPC, 25% PI, and trace amounts of Rh-PE) were generated on poly-carbonate rods of different diameters ranging from approximately 100 nm to 2300 nm. Purified septins were added to supported lipid bilayers at saturating concentrations (from 50 nM to 500 nM) and imaged using scanning electron microscopy (SEM). (A-C) Representative

images of septin filament alignment on rods from the three different categories at 50 nM septin concentration. (A) Rod diameter = 200 nm (B) Rod diameter = 560 nm (C) Rod diameter = 1180 nm. Septin filaments align parallel to the axis of zero curvature on rod diameters ranging from 100-400 nm (higher curvatures). (B) Septins are display various orientations on rod diameters ranging from 417-616 nm in diameter. (C) Septin filaments align along the axis of principal curvature on rod diameters ranging from 630-2300 nm. Scale bars represent 100 nm (A-C). (D) Box and whisker quantification of septin filament orientation on measure rod diameters/curvatures at several septin concentrations (50 nM, 100 nM, 250 nM, and 500 nM). The number of filament orientations measured per rod ranged > 10 filaments. Quantification is from 49 rods. All measured filaments were greater than 100 nm (3 octamers) in length. Black bars represent the median. Error bars are standard deviations.

Figure 4. Single septin complexes have a higher association rate for optimal membrane curvatures

(A) Supported lipid bilayers (75% DOPC and 25% PI) were reconstituted on curvatures of 2 μm^{-1} or 0.67 μm^{-1} and flowed between two polyethylene-glycol (PEG, black) coated coverslips (top coverslip not shown). Non-polymerizable septin complexes were then flowed into the chamber and septin binding and unbinding events were observed using near TIRF microscopy. (B) Representative images of a binding event on κ= 2 μm^{-1} (1 µm bead). Line scan through the particle shows signal intensity as a function of distance and is fit to a Gaussian function. (C-D) Dwell time histograms for membrane curvature of 2 μm^{-1} and 0.67μm^{-1}, respectively. Data were fit to an exponential function. (E) Box and whisker plot quantifying association rate of non-polymerizable septin complexes onto both curvatures (κ =2μm^{-1} and 0.67μm^{-1}). Black bars represent the median. Error bars are standard deviations. N_{beads} = 10 (for κ =2μm^{-1} and 0.67μm^{-1}) $N_{binding\ events}$ = 844 and 315 for for κ =2μm^{-1} and 0.67μm^{-1}, respectively.

Figure 5. Septins have conserved amphipathic helices at their C-termini

(A) Schematic of domains within the yeast septin, Cdc12. PBD (blue): polybasic domain; GTP-BD (green): GTP-binding domain; SUE (purple): Septin unique element; CTE(pink): C-terminal extension; CTE(magenta): coiled-coil domain (red); AH domain (cyan). The AH domain is shown as a helical wheel corresponding primary sequences for wild-type Cdc12 and Cdc12-6 shown below. (B) Selected amphipathic helicies found in the C-terminal extensions of septins in *D. melanogaster*, *C. elegans*, *S. cerevisiae*, and *H. sapiens*, represented through helical wheel diagrams. (C) 1nM of purified wild-type septin complexes (panel 1) and *cdc12-6* septin complexes (panel 2) adsorption (green) onto supported lipid bilayers (magenta) with curvatures of 2 μm^{-1}, 0.67 μm^{-1}, and 0.4 μm^{-1}. Cartoons of septin complexes. Stars highlight cdc12-6 mutation. (D) Box and whisker plot quantifying adsorption of wild-type or *cdc12-6* septin complexes onto supported lipid bilayers of various curvature. Black bars represent the median. Error bars represent the standard deviation. n > 50 beads for each curvature. (E) 2 µM of 2x-Cdc12 AH-GFP binding onto membrane curvatures of 6.67 μm^{-1}, 4 μm^{-1},2 μm^{-1}, 0.67 μm^{-1}, and 0.4 μm^{-1}. (F) Box and whisker plot quantification of 2x-Cdc12 AH-GFP adsorption onto membrane curvatures. Black bars represent the median. Error bars at each curvature are standard deviations for n> 100 beads. (G) Cdc3-mCherry wild-type and Cdc3-mCherry *cdc12-6* strains were treated with alpha-factor and were incubated at either permissive (22 degrees) or restrictive (37 degrees) temperatures for 2 hours. Images are maximum projections. Scale bar is 5 µm

Supplemental Figure legends

S.1. Imaging single septin complexes onto curved membranes using near TIRF microscopy. Schematic of imaging setup. Non-polymerizable septins and SLBs with bead diameters of 1 µm or 3 µm were flowed between two polyethyleneglycol-coated-coverslip and imaged via near TIRF microscopy (A). Two-step photobleaching profile for a single septin complex (B). Timelapse imaging of single molecule binding to a 1 µm bead (C-E). A single septin complex is bound to the bead. (C). A second septin complex binds to the bead, adjacent to the initially bound septin particle. (D). A single septin particle disassociates from the bead (E). Signal intensity profiles for (C-E) were all fit to Gaussian distributions.

S.2. Purification of cdc12-6 and 2x AH domain.
(A). Coomassie staining of recombinantly expressed 2xCdc12 AH-GFP. (B). Coomassie staining of recombinant expressed yeast septins Cdc11-GFP, Cdc3, Cdc12-6, Cdc10 after cleavage of 6xHIS tag via TEV-protease.

S.3. Septin amphipathic helices net charge and hydrophobicity
(A-B). Net charge and hydrophobic moment of selected amphipathic helices, respectively. (C) Phylogenetic tree and sequence alignment of septin amphipathic helices.

Literature Cited

Bertin, A. *et al.* (2008) 'Saccharomyces cerevisiae septins: Supramolecular organization of heterooligomers and the mechanism of filament assembly', *Proceedings of the National Academy of Sciences*. doi: 10.1073/pnas.0803330105.

Bridges, A. A. *et al.* (2016) 'Micron-scale plasma membrane curvature is recognized by the septin cytoskeleton', *Journal of Cell Biology*. doi: 10.1083/jcb.201512029.

Byers, B. and Goetsch, L. E. (1976) 'A highly ordered ring of membrane-associated filaments in budding yeast', *Journal of Cell Biology*. doi: 10.1083/jcb.69.3.717.

Cannon, K. S., Woods, B. L. and Gladfelter, A. S. (2017) 'The Unsolved Problem of How Cells Sense Micron-Scale Curvature', *Trends in Biochemical Sciences.* doi: 10.1016/j.tibs.2017.10.001.

Chen, Z. *et al.* (2016) 'The N-Terminal Amphipathic Helix of Endophilin Does Not Contribute to Its Molecular Curvature Generation Capacity', *Journal of the American Chemical Society*. doi: 10.1021/jacs.6b06820.

Cho, S. J. *et al.* (2011) 'Septin 6 regulates the cytoarchitecture of neurons through localization at dendritic branch points and bases of protrusions', *Molecules and Cells*. doi: 10.1007/s10059-011-1048-9.

Clay, L. *et al.* (2014) 'A sphingolipid-dependent diffusion barrier confines ER stress to the yeast mother cell', *eLife*. doi: 10.7554/eLife.01883.

DeMay, B. S. *et al.* (2009) 'Regulation of distinct septin rings in a single cell by Elm1p and Gin4p kinases.', *Molecular biology of the cell*. doi: 10.1091/mbc.E08-12-1169.

Drin, G. *et al.* (2007) 'A general amphipathic α-helical motif for sensing membrane curvature', *Nature Structural and Molecular Biology*. doi: 10.1038/nsmb1194.

Drin, G. and Antonny, B. (2010) 'Amphipathic helices and membrane curvature', *FEBS Letters*. doi: 10.1016/j.febslet.2009.10.022.

Field, C. M. *et al.* (1996) 'A purified Drosophila septin complex forms filaments and exhibits GTPase activity', *Journal of Cell Biology*. doi: 10.1083/jcb.133.3.605.

Finnigan, G. C. *et al.* (2015) 'The carboxy-terminal tails of septins Cdc11 and Shs1 recruit myosin-II binding factor Bni5 to the bud neck in Saccharomyces cerevisiae', *Genetics.* doi: 10.1534/genetics.115.176503.

Ford, S. K. and Pringle, J. R. (1991) 'Cellular morphogenesis in the Saccharomyces cerevisiae cell cycle: Localization of the CDC11 gene product and the timing of events at the budding site', *Developmental Genetics*. doi: 10.1002/dvg.1020120405.

Frazier, J. A. *et al.* (1998) 'Polymerization of purified yeast septins: Evidence that organized filament arrays may not be required for septin function', *Journal of Cell Biology*. doi: 10.1083/jcb.143.3.737.

Garcia, G. *et al.* (2011) 'Subunit-dependent modulation of septin assembly: Budding yeast septin Shs1 promotes ring and gauze formation', *Journal of Cell Biology*. doi: 10.1083/jcb.201107123.

Gill, R. L. *et al.* (2015) 'Structural basis for the geometry-driven localization of a small protein', *Proceedings of the National Academy of Sciences.* doi: 10.1073/pnas.1423868112.

Giot, L. and Konopka, J. B. (1997) 'Functional analysis of the interaction between Afr1p and the Cdc12p septin, two proteins involved in pheromone-induced morphogenesis', *Mol Biol Cell*. doi: 10.1091/mbc.8.6.987.

Gladfelter, A. S. *et al.* (2005) 'Interplay between septin organization, cell cycle and cell shape in yeast.', *Journal of cell science.* doi: 10.1242/jcs.02286.

Haarer, B. K. and Pringle, J. R. (1987) ‘Immunofluorescence localization of the Saccharomyces cerevisiae CDC12 gene product to the vicinity of the 10-nm filaments in the mother-bud neck.’, *Molecular and cellular biology*. doi: 10.1128/mcb.7.10.3678.
Hatzakis, N. S. *et al.* (2009) ‘How curved membranes recruit amphipathic helices and protein anchoring motifs’, *Nature Chemical Biology*. doi: 10.1038/nchembio.213.
Hussain, S. *et al.* (2018) ‘MreB filaments align along greatest principal membrane curvature to orient cell wall synthesis’, *eLife*. doi: 10.7554/eLife.32471.
John, C. M. *et al.* (2007) ‘The Caenorhabditis elegans septin complex is nonpolar’, *EMBO Journal*. doi: 10.1038/sj.emboj.7601775.
Johnson, C. R. *et al.* (2015) ‘Cytosolic chaperones mediate quality control of higher-order septin assembly in budding yeast’, *Molecular Biology of the Cell*. doi: 10.1091/mbc.E14-11-1531.
Joo, E., Surka, M. C. and Trimble, W. S. (2007) ‘Mammalian SEPT2 Is Required for Scaffolding Nonmuscle Myosin II and Its Kinases’, *Developmental Cell*. doi: 10.1016/j.devcel.2007.09.001.
Kelley, J. B. *et al.* (2015) ‘RGS proteins and septins cooperate to promote chemotropism by regulating polar cap mobility’, *Current Biology*. doi: 10.1016/j.cub.2014.11.047.
Khan, A., Newby, J. and Gladfelter, A. S. (2018) ‘Control of septin filament flexibility and bundling by subunit composition and nucleotide interactions’, *Molecular Biology of the Cell*. doi: 10.1091/mbc.E17-10-0608.
Kim, E. Y. *et al.* (2017) ‘Dash-and-Recruit Mechanism Drives Membrane Curvature Recognition by the Small Bacterial Protein SpoVM’, *Cell Systems*. doi: 10.1016/j.cels.2017.10.004.
Longtine, M. S. *et al.* (2000) ‘Septin-Dependent Assembly of a Cell Cycle-Regulatory Module in Saccharomyces cerevisiae’, *Molecular and Cellular Biology*. doi: 10.1128/MCB.20.11.4049-4061.2000.
Maddox, A. S. *et al.* (2007) ‘Anillin and the Septins Promote Asymmetric Ingression of the Cytokinetic Furrow’, *Developmental Cell*. doi: 10.1016/j.devcel.2007.02.018.
Madsen, K. L. *et al.* (2010) ‘BAR domains, amphipathic helices and membrane-anchored proteins use the same mechanism to sense membrane curvature’, *FEBS Letters*. doi: 10.1016/j.febslet.2010.01.053.
Matsuzaki, K. (1998) ‘Magainins as paradigm for the mode of action of pore forming polypeptides’, *Biochimica et Biophysica Acta - Reviews on Biomembranes*. doi: 10.1016/S0304-4157(98)00014-8.
Meitinger, F. *et al.* (2011) ‘Phosphorylation-dependent regulation of the F-BAR protein Hof1 during cytokinesis’, *Genes and Development*. doi: 10.1101/gad.622411.
Pan, F., Malmberg, R. L. and Momany, M. (2007) ‘Analysis of septins across kingdoms reveals orthology and new motifs’, *BMC Evolutionary Biology*. doi: 10.1186/1471-2148-7-103.
Pranke, I. M. *et al.* (2011) ‘α-Synuclein and ALPS motifs are membrane curvature sensors whose contrasting chemistry mediates selective vesicle binding’, *Journal of Cell Biology*. doi: 10.1083/jcb.201011118.
Ramamurthi, K. S. *et al.* (2009) ‘Geometric cue for protein localization in a bacterium’, *Science*. doi: 10.1126/science.1169218.
Sadian, Y. *et al.* (2013) ‘The role of Cdc42 and Gic1 in the regulation of septin filament formation and dissociation’, *eLife*. doi: 10.7554/eLife.01085.
Sakchaisri, K. *et al.* (2004) ‘Coupling morphogenesis to mitotic entry.’, *Proceedings of the National Academy of Sciences of the United States of America*. doi: 10.1073/pnas.0400641101.
Simunovic, M. *et al.* (2015) ‘When Physics Takes Over: BAR Proteins and Membrane

Curvature', *Trends in Cell Biology*. doi: 10.1016/j.tcb.2015.09.005.
Simunovic, M., Srivastava, A. and Voth, G. A. (2013) 'Linear aggregation of proteins on the membrane as a prelude to membrane remodeling', *Proceedings of the National Academy of Sciences*. doi: 10.1073/pnas.1309819110.
Sirajuddin, M. *et al*. (2007) 'Structural insight into filament formation by mammalian septins', *Nature*. doi: 10.1038/nature06052.
Spiliotis, E. T., Kinoshita, M. and Nelson, W. J. (2005) 'A mitotic septin scaffold required for mammalian chromosome congression and segregation', *Science*. doi: 10.1126/science.1106823.
Ursell, T. S. *et al.* (2014) 'Rod-like bacterial shape is maintained by feedback between cell curvature and cytoskeletal localization', *Proceedings of the National Academy of Sciences*. doi: 10.1073/pnas.1317174111.
Westfall, P. J. and Momany, M. (2002) 'Aspergillus nidulans septin AspB plays pre- and postmitotic roles in septum, branch, and conidiophore development', *Molecular Biology of the Cell*. doi: 10.1091/mbc.
Yamada, S. *et al.* (2016) 'Septin Interferes with the Temperature-Dependent Domain Formation and Disappearance of Lipid Bilayer Membranes', *Langmuir*. doi: 10.1021/acs.langmuir.6b03452.
Zimmerberg, J. and Kozlov, M. M. (2006) 'How proteins produce cellular membrane curvature', *Nature Reviews Molecular Cell Biology*. doi: 10.1038/nrm1784.

A.

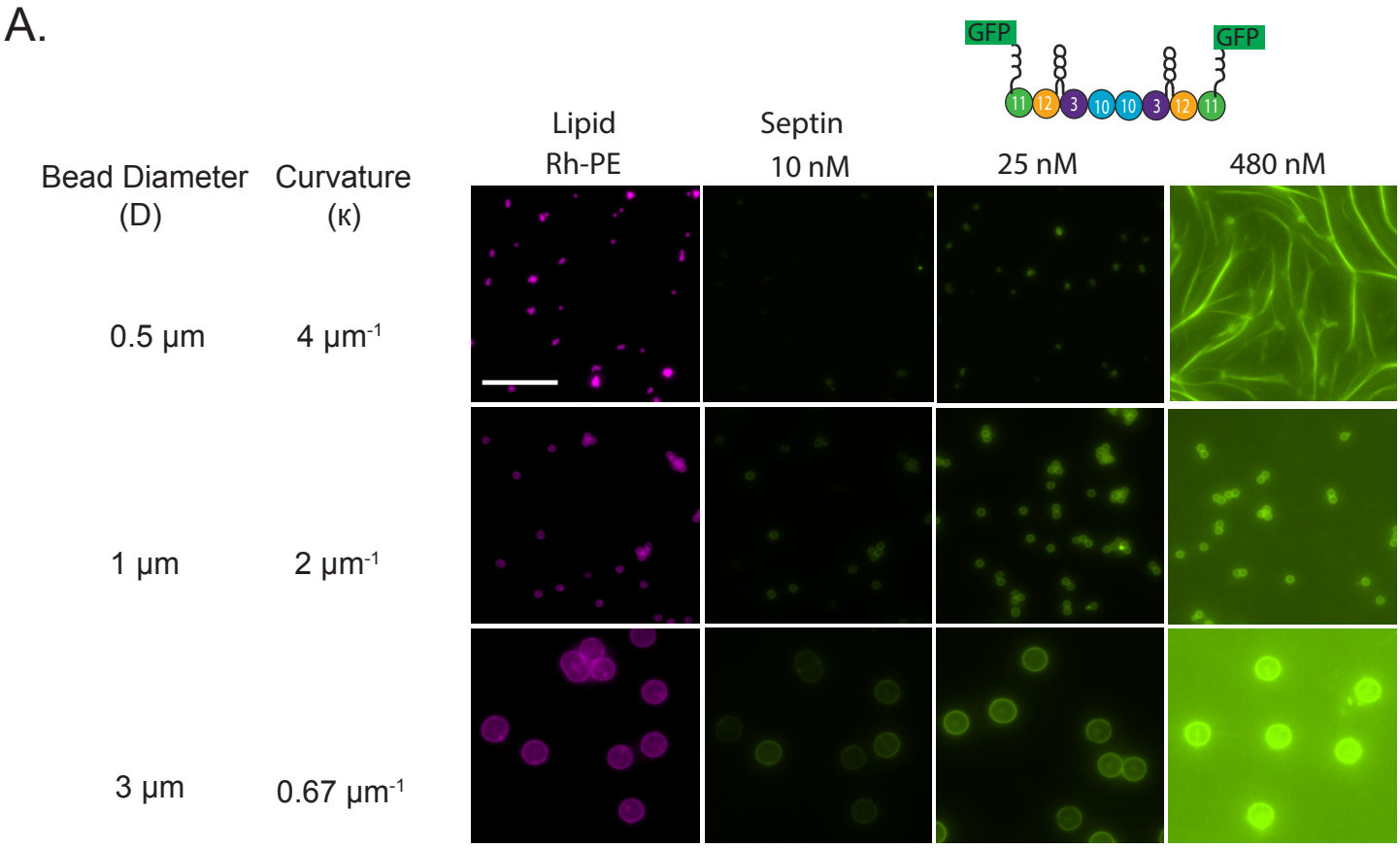
GFP
GFP
11
12
3
10
10
3
12
11
Bead Diameter (D)
Curvature (κ)
Lipid Rh-PE
Septin 10 nM
25 nM
480 nM
0.5 µm
4 µm-1
1 µm
2 µm-1
3 µm
0.67 µm-1

B.

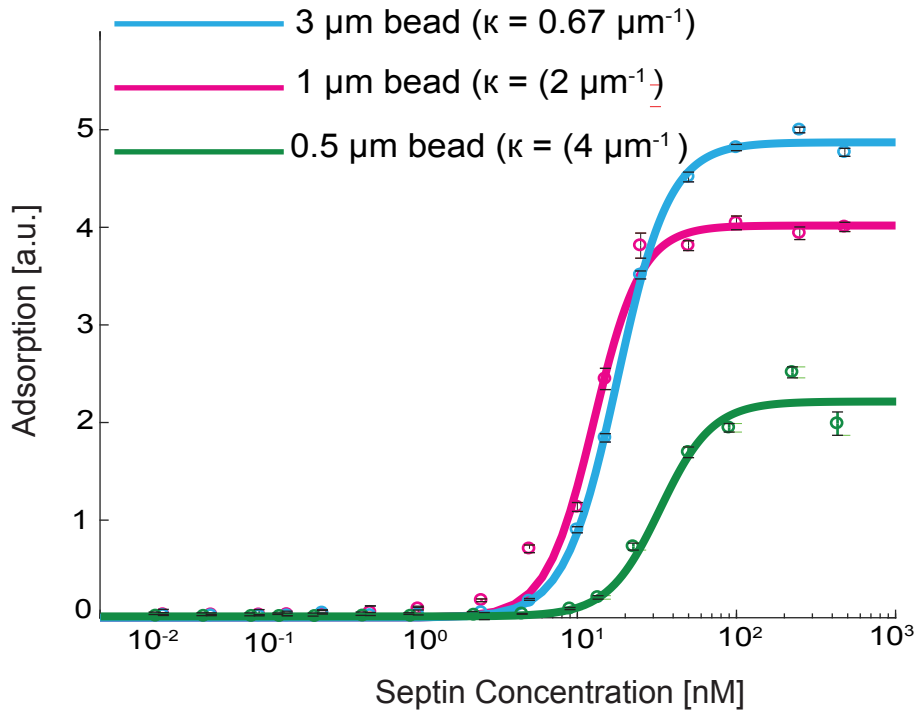
3 µm bead (κ = 0.67 µm-1)
1 µm bead (κ = (2 µm-1)
0.5 µm bead (κ = (4 µm-1)
Adsorption [a.u.]
0
1
2
3
4
5
10-2
10-1
100
101
102
103
Septin Concentration [nM]

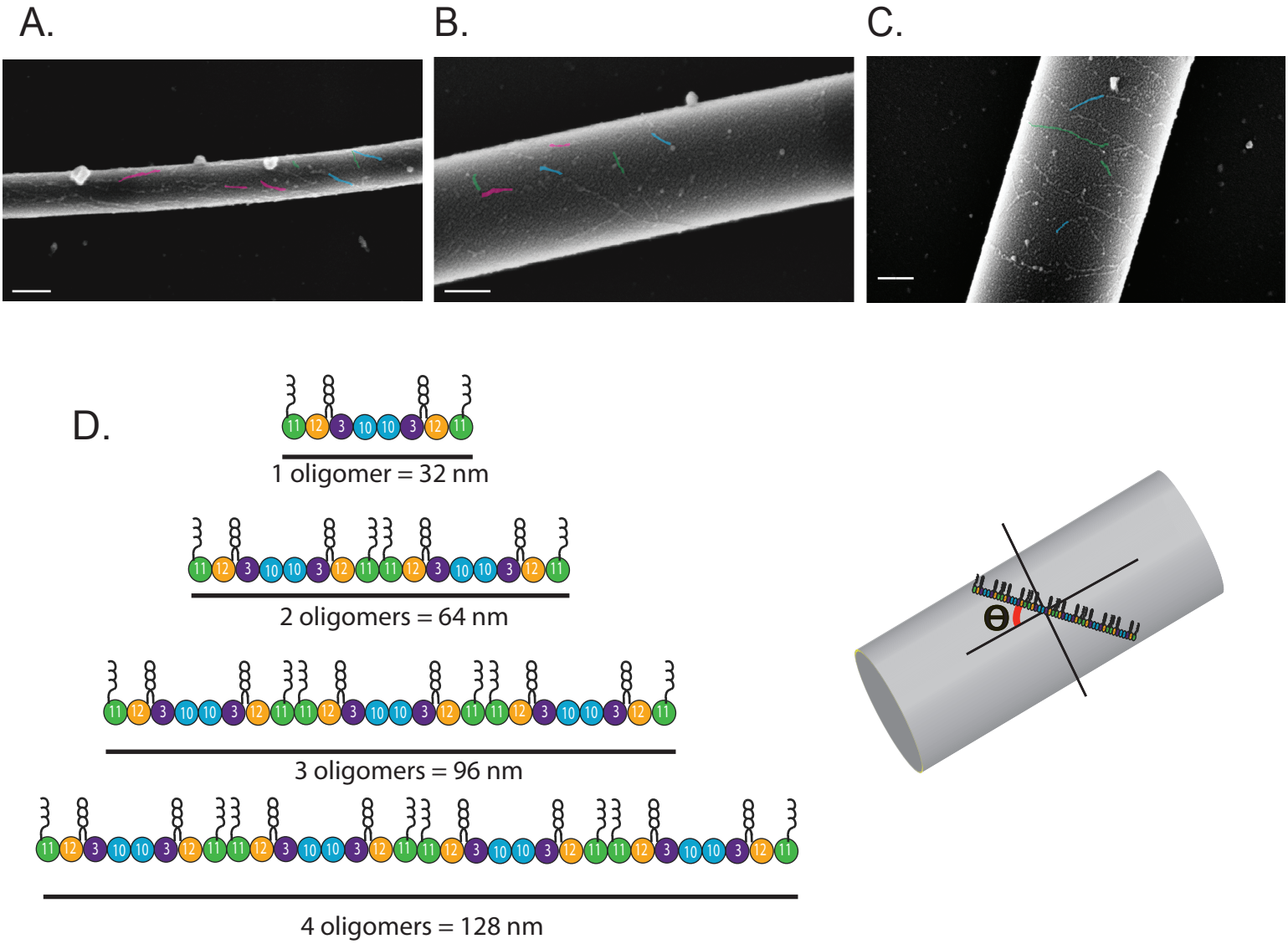
A.
B.
C.
D.
1 oligomer = 32 nm
2 oligomers = 64 nm
3 oligomers = 96 nm
4 oligomers = 128 nm
θ
E.
F.
G.
Theta
Octamer Number

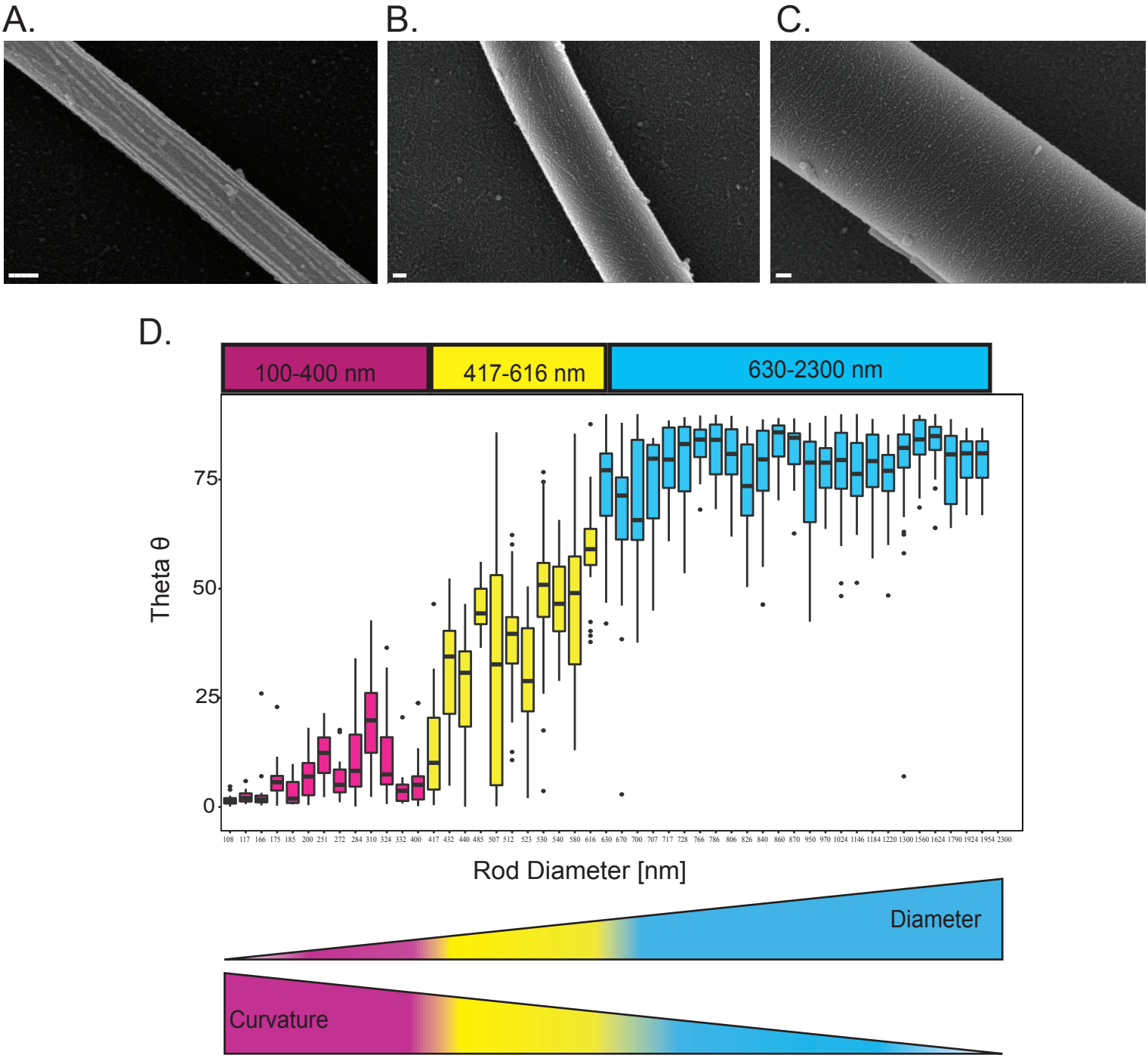
A.
B.
C.
D.
100-400 nm
417-616 nm
630-2300 nm
Theta θ
0
25
50
75
108 117 166 175 185 200 251 272 284 310 324 332 400 417 432 440 485 507 512 523 530 540 580 616 630 670 700 707 717 728 766 786 806 826 840 860 870 950 970 1024 1146 1184 1220 1300 1560 1624 1790 1924 1954 2300
Rod Diameter [nm]
Diameter
Curvature

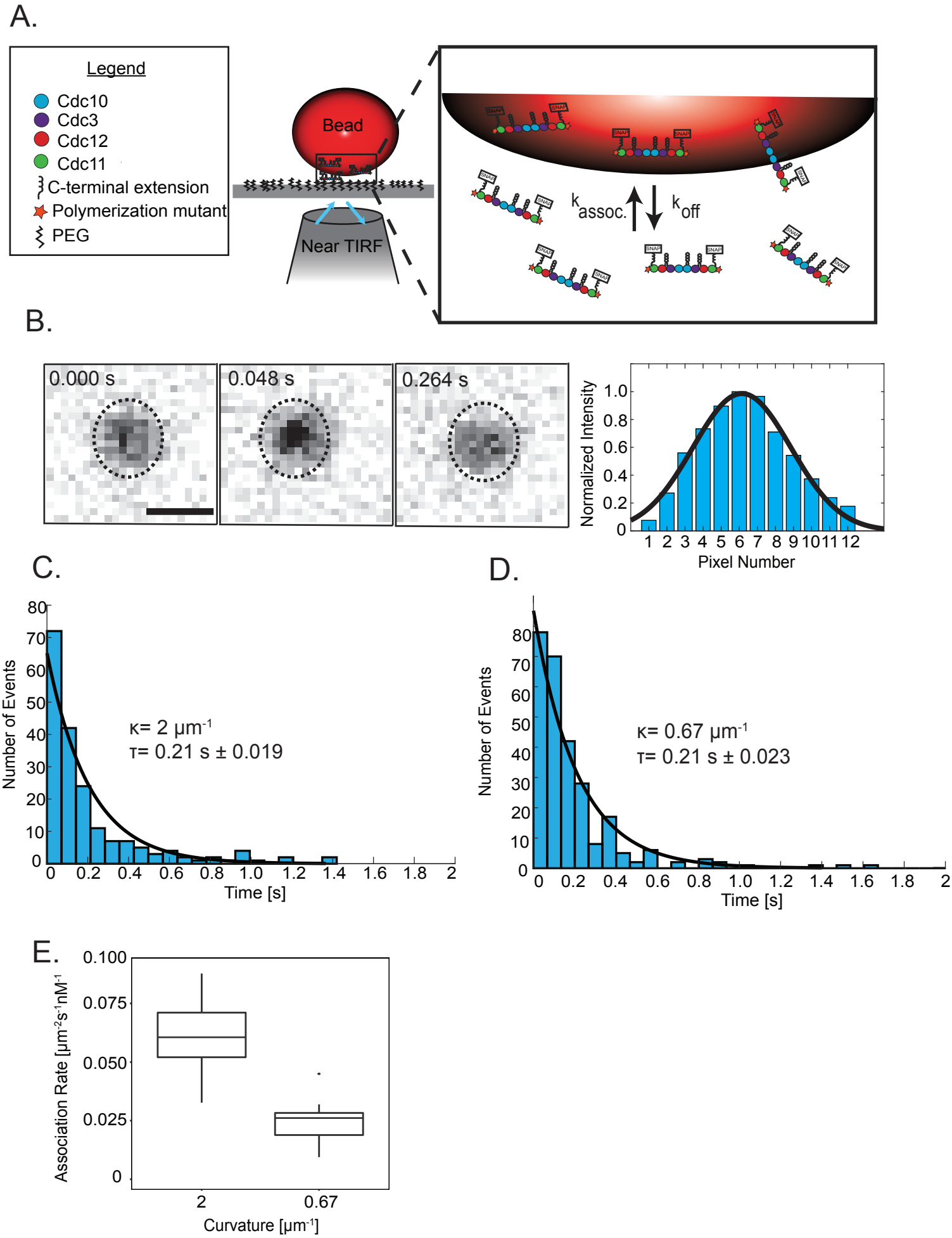
A.
Legend
Cdc10
Cdc3
Cdc12
Cdc11
C-terminal extension
Polymerization mutant
PEG
Bead
Near TIRF
SNAP
k assoc.
k off
B.
0.000 s
0.048 s
0.264 s
Normalized Intensity
Pixel Number
C.
Number of Events
κ= 2 μm-1
τ= 0.21 s ± 0.019
Time [s]
D.
Number of Events
κ= 0.67 μm-1
τ= 0.21 s ± 0.023
Time [s]
E.
Association Rate [μm-2s-1nM-1]
Curvature [μm-1]

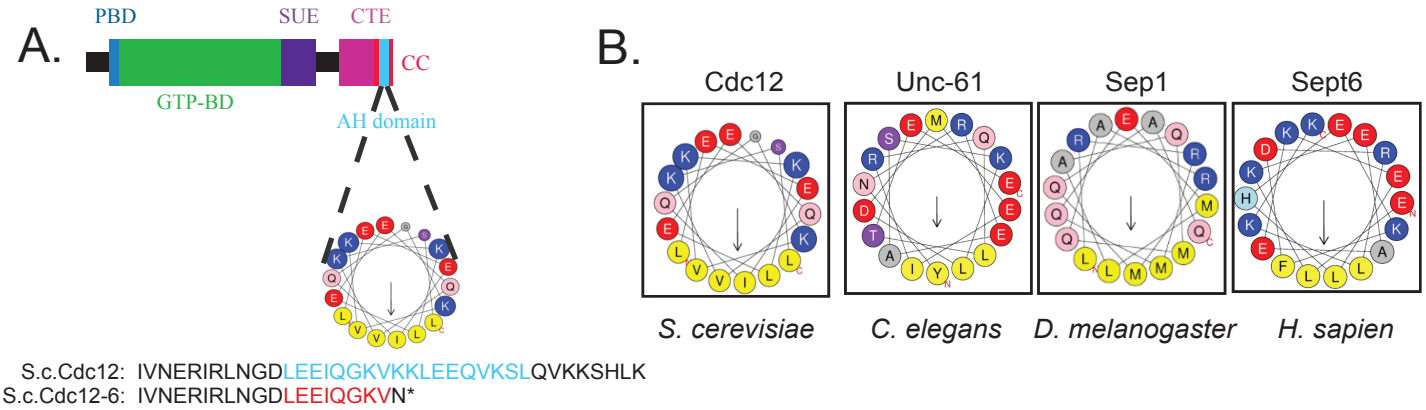

S.c.Cdc12: IVNERIRLNGDLEEIQGKVKKLEEQVKSLQVKKSHLK
S.c.Cdc12-6: IVNERIRLNGDLEEIQGKVN*

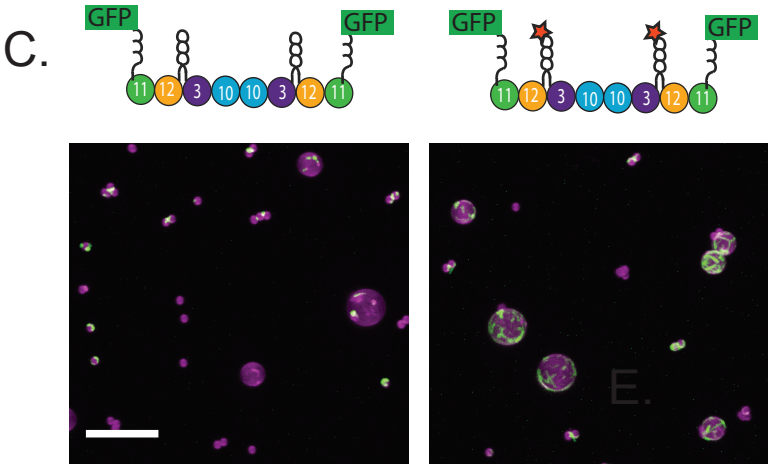

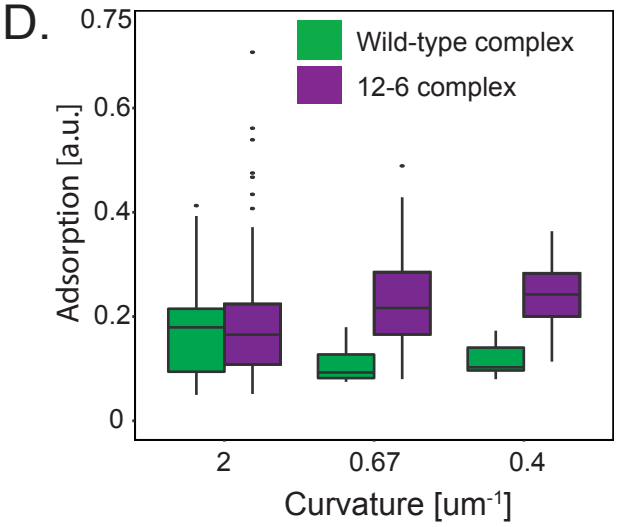

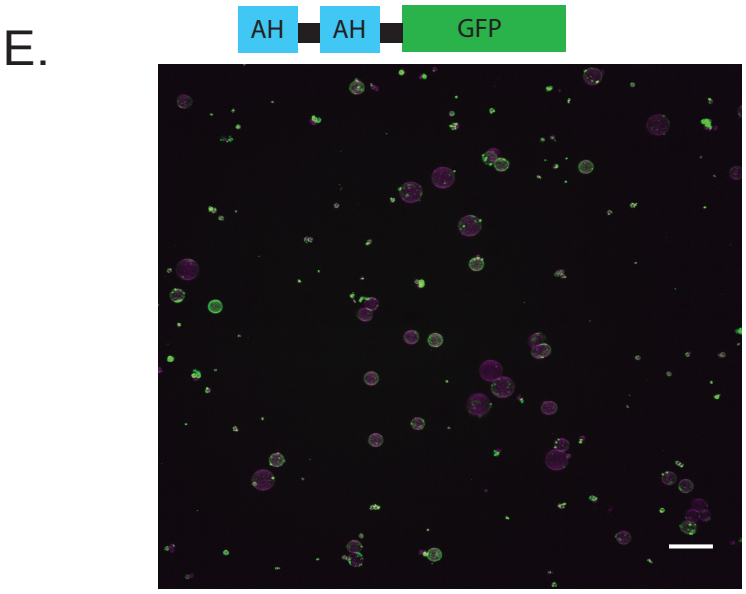

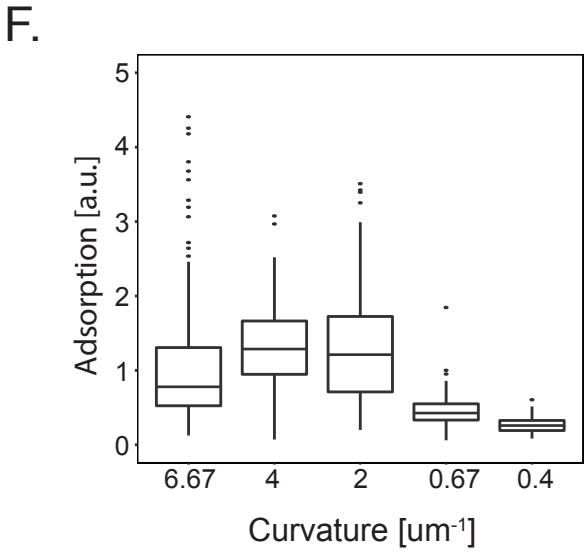

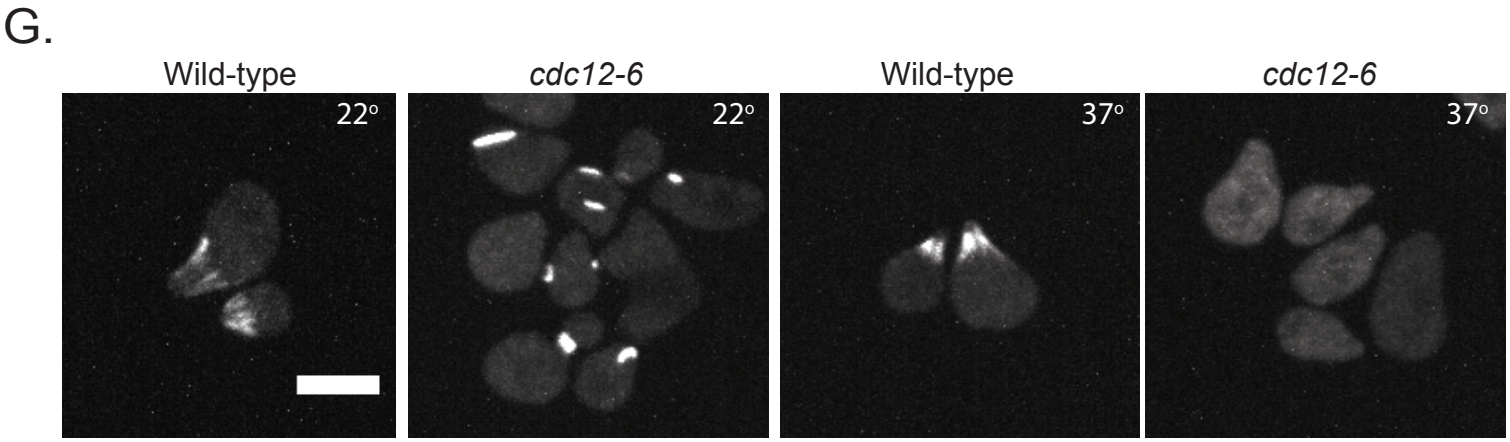

Table 1. Biochemical parameters for septin adsorption onto various membrane curvatures

Curvature [μm^{1}]	4	2	0.67
Kd [nM]	34.3 ± 6.0	13.5 ± 0.78	18.5 ± 1.39
B_{max} [a.u]	2.2 ± 0.3	4.0 ± 0.197	4.8 ± 0.07
Hill Coefficient	2.6 ± 0.8	2.9 ± 0.8	2.6 ± 0.2

Table 2. Coefficient of variation for septin filament alignment on rods

Septin Concentration	Rod Diameter		
	100-400 nm	401-600 nm	> 600 nm
25 nM	0.73	0.48	0.40
50 nM	0.94	0.58	0.10
100 nM	0.65	0.53	0.12
250 nM	1.05	0.59	0.17
500 nM	1.04	0.23	0.18